

PMPBench: A Paired Multi-Modal Pan-Cancer Benchmark for Medical Image Synthesis

Yifan Chen^{1,*} Fei Yin^{1,*} Hao Chen^{1,*} Jia Wu² Chao Li^{1,3}

¹University of Cambridge ²MD Anderson Cancer Center ³University of Dundee

yifanchencam@gmail.com

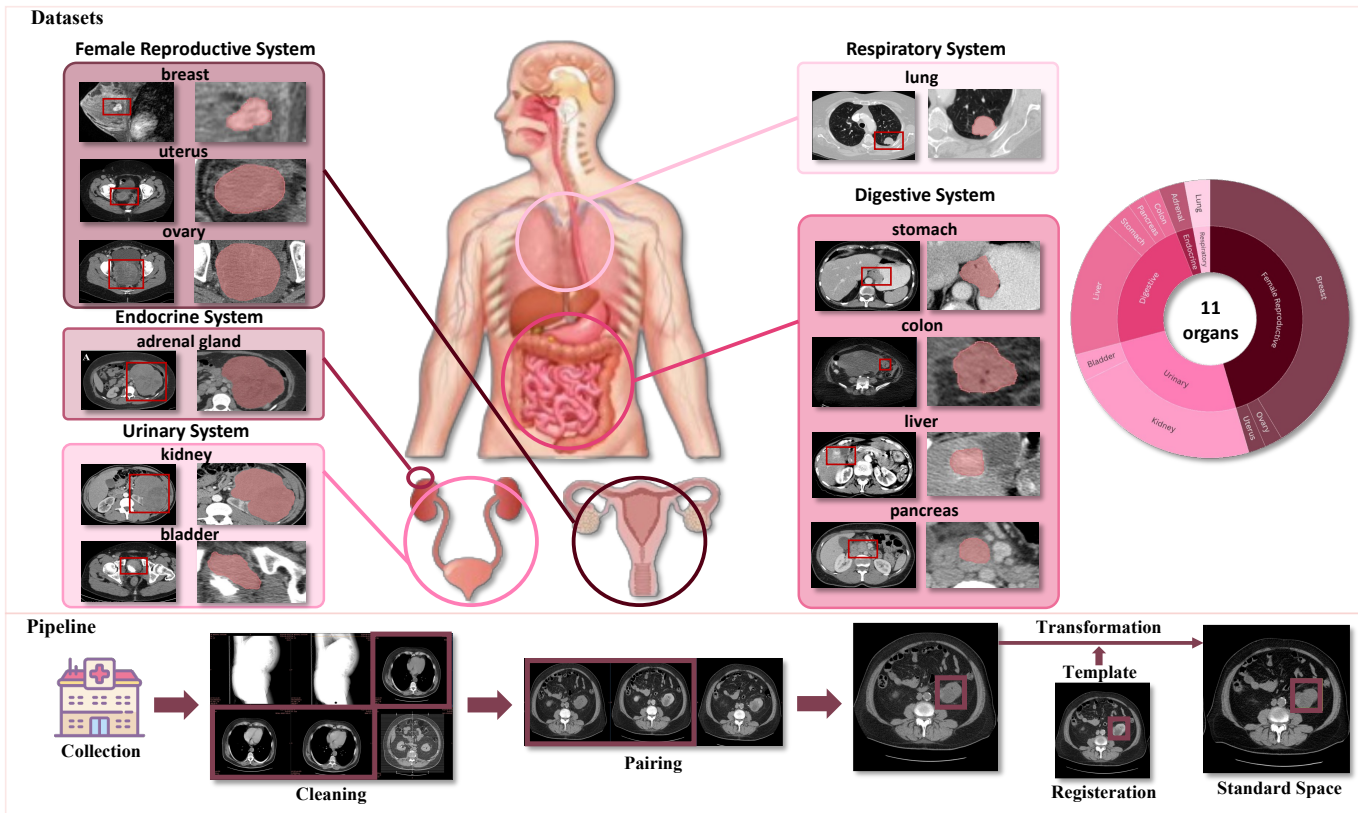


Fig. 1: *Top:* representative organ-system with paired contrast and non-contrast scans. The charts imply organ-wise composition and modality balance. *Bottom:* standardized curation pipeline including data collection, cleaning, pairing, and registration.

Abstract—Contrast medium plays a pivotal role in radiological imaging, as it amplifies lesion conspicuity and improves detection for the diagnosis of tumor-related diseases. However, depending on the patient’s health condition or the medical resources available, the use of contrast medium is not always feasible. Recent work has explored AI-based image translation to synthesize contrast-enhanced images directly from non-contrast scans, aims to reduce side effects and streamlines clinical workflows. Progress in this direction has been constrained by data limitations: (1) existing public datasets focus almost exclusively on brain-related paired MR modalities; (2) other collections include partially paired data but suffer from missing modalities/timestamps and imperfect spatial alignment; (3) explicit labeling of CT vs. CTC or DCE phases is often absent; (4) substantial resources remain private. To bridge this gap, we introduce the first public, fully paired, pan-cancer medical imaging dataset spanning

11 human organs. The MR data include complete dynamic contrast-enhanced (DCE) sequences covering all three phases (DCE1–DCE3), while the CT data provide paired non-contrast and contrast-enhanced acquisitions (CTC). The dataset is curated for anatomical correspondence, enabling rigorous evaluation of $1 \rightarrow 1$, $N \rightarrow 1$, and $N \rightarrow N$ translation settings (e.g., predicting DCE phases from non-contrast inputs). Built upon this resource, we establish a comprehensive benchmark. We report results from representative baselines of contemporary image-to-image translation. We release the dataset and benchmark to catalyze research on safe, effective contrast synthesis, with direct relevance to multi-organ oncology imaging workflows. Our code and dataset are publicly available at <https://github.com/YifanChen02/PMPBench>.

Index Terms—benchmark, paired, image translation, pan-cancer

* Yifan Chen, Fei Yin and Hao Chen contribute equally.

I. INTRODUCTION

Accurate diagnosis from medical images often depends on how clearly subtle tissue differences can be visualized. Contrast medium amplifies these differences by highlighting lesions and vascular structures, thereby improving the sensitivity and reliability of tumor detection. Yet their use is not always feasible: certain patients face health risks from contrast administration, and resource limitations can further restrict availability. Consequently, many scans are acquired without contrast enhancement, leaving clinicians with incomplete diagnostic information.

Recent advances in generative AI [1]–[3] offer promising solutions by synthesizing contrast-enhanced images directly from non-contrast scans [4], [5]. Such approaches open the door to safer imaging protocols and streamlined clinical workflows. However, their development critically depends on access to large-scale, well-curated paired datasets spanning diverse organs and cancer types.

Existing resources remain inadequate. (1) Publicly available paired MRI datasets, such as BraTS [6], are almost exclusively limited to brain imaging. (2) Other collections, including AMOS [7] or datasets from TCIA [8], provide partially paired CT and MRI data but suffer from missing modalities, timestamps, or imperfect spatial alignment. (3) Explicit annotations distinguishing non-contrast CT from contrast-enhanced CT (CTC) or delineating dynamic contrast-enhanced (DCE) MRI phases are often absent, as in CT-ORG [9]. (4) Finally, substantial multi-organ resources cohorts remain private, limiting community-wide benchmarking.

To bridge this gap, we introduce PMPBench, the first *public, fully paired, pan-cancer* dataset covering 11 human organs. It provides complete dynamic contrast-enhanced magnetic resonance imaging (DCE-MRI) sequences (DCE1–DCE3), alongside paired non-contrast and contrast-enhanced computed tomography (CT / CTC). All data are carefully curated for anatomical correspondence, enabling systematic evaluation of image translation tasks under $1 \rightarrow 1$, $N \rightarrow 1$, and $N \rightarrow N$ settings.

Building upon this resource, we establish a comprehensive benchmark by evaluating representative baseline methods in image-to-image translation, including GAN-based [1], [10] and diffusion-based [11], [12] models. Beyond these baselines, we further explore the emerging flow matching [13], [14] paradigm, which unifies the advantages of likelihood-based training and stable deterministic generation. We introduce FlowMI, a flow-based missing modality imputation model. Unlike former image-to-image translation frameworks [10], [15]–[17], which assume complete modality availability, our approach explicitly addresses the missing-modality setting. FlowMI projects both complete and incomplete modalities into a shared latent space through modality-specific encoders combined via a product-of-experts aggregation. It then learns a continuous flow that transforms the resulting “broken” latent codes to their fully observed counterparts. This design allows robust reconstruction under arbitrary missing patterns and

achieves superior performance in recovering details. Notably, the ability to recover fine-grained details is critical for downstream clinical tasks such as tumor detection. Together, the dataset, benchmark, and FlowMI establish a strong foundation for advancing safe and effective contrast synthesis. Our key contributions are summarized as follows:

1. We present the first *public, fully paired* contrast-enhanced and non-contrast, *pan-cancer* dataset, providing a large-scale, high-quality resource to facilitate medical imaging research.
2. We propose FlowMI, a flow-matching model that captures complex cross-modality relationships and leverages an uncertainty mitigation strategy, leading to more reliable multimodal image synthesis with improved potential for downstream clinical applications.
3. We conduct a comprehensive benchmark across diverse organs, modalities, and translation tasks, establishing strong reference results for future research. Our proposed FlowMI achieves consistently superior performance across settings.

II. PMPBENCH: DESIGN AND CONSTRUCTION

In this section, we first define the task enabled by PMPBench (section II-A). We then describe the data curation and preparation process (section II-B), followed by a quantitative analysis of the quality and diversity of PMPBench (section II-C). Finally, we compare our dataset against existing benchmarks (section II-D) to highlight its unique advantages.

A. Task Definition

Generative models for medical image translation aim to model complex anatomical structures, capture modality-specific features, and learn cross-modality mappings. Formally, given a set of input modalities $X = \{x_1, x_2, \dots, x_n\}$ and one or more target modalities $Y = \{y_1, y_2, \dots, y_m\}$, a generative model f produces synthesized images \hat{Y} that approximate the ground-truth targets Y :

$$\hat{Y} = f(X). \quad (1)$$

In this study, we consider several widely used imaging modalities: Computed Tomography (CT), contrast-enhanced CT (CTC), and multiple Magnetic Resonance Imaging (MRI) sequences, including Dynamic Contrast-Enhanced MRI (DCE).

To comprehensively evaluate different generative models, we design benchmark tasks that reflect both increasing levels of difficulty and common clinical scenarios of missing modalities. As illustrated in fig. 2, we consider three representative settings:

1-to-1 Translation: Single input modality to a single target (e.g., CT \rightarrow CTC or DCE₁ \rightarrow DCE₂). This setting tests a model’s ability to capture modality-specific features and preserve one-to-one anatomical correspondences.

N-to-1 Translation: Multiple input modalities to a single target (e.g., DCE₁, DCE₃ \rightarrow DCE₂). This evaluates how well models integrate complementary anatomical information across sequences while maintaining structural fidelity and modality consistency. In DCE imaging, this setting further corresponds to reconstructing an intermediate phase from its

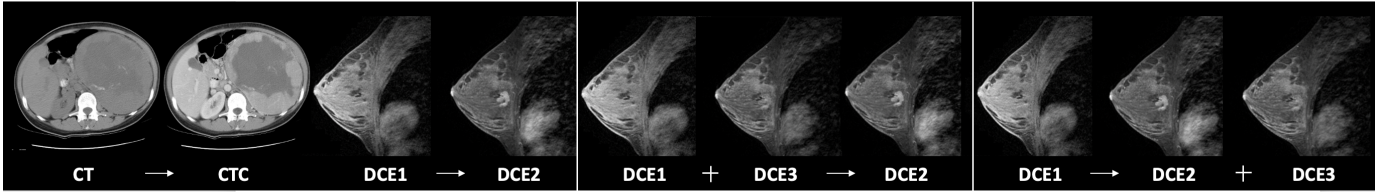


Fig. 2: Representative task settings with examples. (a) CT → CTC (1→1), (b) DCE₁ → DCE₂ (1→1), (c) DCE_{1, 3} → DCE₂ (N→1), (d) DCE₁ → DCE_{2, 3} (1→N).

neighbors, thereby probing whether models can capture the temporal dynamics of contrast uptake.

1-to-N Translation: A single input modality to multiple targets simultaneously (e.g., DCE₁ → DCE₂, DCE₃). This setting assesses whether models can jointly capture inter-modal dependencies and generate anatomically consistent outputs across domains. Clinically, it is relevant for scenarios where only an early phase or a non-contrast scan is acquired, and later phases must be synthesized to approximate the full dynamic sequence.

Together, these tasks can be unified under the general **N-to-N translation** formulation, where both input and output may consist of multiple modalities. They span a spectrum from fundamental to highly challenging scenarios, ensuring that our benchmark is representative of real-world clinical requirements for missing modality synthesis.

B. Dataset Curation and Preparation

A major obstacle for contrast synthesis research is the lack of large-scale, paired datasets spanning multiple organs and imaging modalities. To address this, we curated PMPBench, a multi-organ, pan-cancer resource constructed entirely from publicly available sources.

PMPBench distinguishes itself by providing: (i) explicit pairing of contrast-enhanced (CE) and non-contrast-enhanced (NCE) scans across both CT and MRI, and (ii) broad coverage of clinically relevant organs frequently encountered in oncology. As illustrated in fig. 1, the curation process consists of dataset selection, quality filtering, and standardized preprocessing to ensure anatomical correspondence and clinical validity.

Targeted organs and imaging modalities. Based on three criteria—(i) availability of paired CE/NCE scans, (ii) prevalence in oncology imaging studies, and (iii) the clinical importance of contrast enhancement for lesion delineation—we selected 11 organs spanning both CT(adrenal gland, ovary, uterus, stomach, pancreas, liver, colon, bladder, kidney, lung) and MRI(breast).

Data selection and quality filtering. All scans were sourced from publicly available repositories such as The Cancer Imaging Archive (TCIA) and related datasets (e.g., TCGA, CPTAC, CMB, UCSF, I-SPY). We identified collections with paired CE/NCE scans or reliable metadata indicating contrast phase, retrieved the raw DICOM/NIFTI files, and excluded studies with severe artifacts, incomplete coverage, or corrupted files. This multi-stage filtering ensured that only scans with reliable

contrast information and sufficient anatomical coverage were retained for preprocessing.

Preprocessing with clinical validation. To harmonize diverse sources into a unified benchmark, we applied a standardized pipeline:

Contrast-pair identification: automated metadata parsing (SeriesDescription, ContrastBolusAgent, AcquisitionTime) was used to distinguish CE/NCE scans.

Validation and quality control: annotators verified preliminary CE/NCE modalities and overall image quality, discarding ambiguous or low-quality cases. All annotation and validation procedures were conducted by a team of trained annotators led by a board-certified radiologist with oncology specialization, ensuring both clinical accuracy and ethical compliance. Final confirmation was provided by the radiologist, who explicitly labeled CT vs. CTC and identified DCE time steps.

Registration: rigid and affine alignment between CE and NCE scans was performed using the 3D Slicer Elastix [18] module, followed by deformable B-spline registration for motion-prone organs (e.g., liver, lung). The ITK–Elastix backend was adopted with mutual-information metrics and a multi-resolution pyramid schedule. Detailed parameter configurations are provided in the supplementary material.

Cropping and resampling: organ-level bounding box cropping and resampling to isotropic spacing (1×1×1 mm).

Normalization: For CT, hounsfield Unit (HU) windowing per organ (e.g., soft tissue: [−200, 300] HU), then min–max normalization. For MRI, z-score normalization per scan is used to mitigate inter-patient intensity variation.

Pairing verification: final visual inspection to ensure anatomical correspondence between CE and NCE scans.

C. Data Statistics and Division

The PMPBench collection is organized hierarchically: first by imaging modality (Magnetic Resonance, MR; Computed Tomography, CT), and then by organ-specific groups. In total, the dataset spans 11 organs grouped into 6 subsets representing 5 anatomical systems: Endocrine (adrenal), Digestive (stomach, pancreas, liver, colon), Urinary (bladder, kidney), Respiratory (lung), and Female Reproductive (uterus, ovary, and breast).

Across these organs, the dataset covers 19 cancer types, including: adrenocortical carcinoma (adrenal); ovarian serous cystadenocarcinoma (ovary); uterine corpus endometrial carcinoma (uterus); stomach adenocarcinoma (stomach); ductal adenocarcinoma and hepatocellular carcinoma (liver); colon

TABLE I: A comparison of our proposed PMPBench to other benchmarks.

Benchmarks	Organ	MR	CT	Paired	Size	Application
CHAOS [19]	Abdomen	✓	✓		120	Healthy abdominal organ research
BraTS 2025 [20]	Brain	✓		✓	4425	Brain tumor research
IXI [21]	Brain	✓			600	Healthy brain research
crossMoDA [22]	Ear	✓			379	Cochlear implant research
ACDC [23]	Cardiac	✓			150	Cardiac diagnosis
MMWHS [24]	Cardiac	✓	✓		120	Cardiac research
FDG-PET/CT [25]	Whole body	✓	✓		1014	Tumor, lung cancer research
Ours	Adrenal, Breast, Bladder, Colon, Kidney, Liver, Lung, Ovary, Pancreas, Stomach, Uterus	✓	✓	✓	2642	Pan-cancer research

adenocarcinoma and colorectal cancer (colon); bladder urothelial carcinoma (bladder); kidney renal clear cell, papillary cell, and chromophobe carcinomas (kidney); lung adenocarcinoma and squamous cell carcinoma (lung); and breast carcinoma (breast). A detailed breakdown of case numbers per organ, modality, and cancer type is provided in the supplementary.

For benchmarking, the dataset is split into training (70%), validation (10%), and test (20%) sets. Stratified sampling ensures proportional representation across organ systems and cancer types. The test set is further subdivided into a *test-mini* split (5% of the full dataset), designed for rapid validation while preserving the distribution of the complete test set. Unless otherwise specified, all reported results are based on the *test-mini* split.

D. Comparisons with Existing Benchmarks

We position PMPBench against representative public benchmarks along five axes relevant for multimodal image translation and missing-modality synthesis: (i) organ/system coverage, (ii) imaging modalities (MR/CT and contrast availability), (iii) explicit CE–NCE pairing at the *per-patient* level, (iv) dataset scale and balance, and (v) primary application focus. Table I summarizes the comparison.

Brain-centric MR benchmarks. Resources such as BraTS [6], BraSyn [26], IXI [21], OASIS-3 [27], and ADNI [28] provide large-scale brain MRI data, supporting tumor segmentation and neurodegeneration studies. However, they are *single-organ* and typically lack explicit CE–NCE pairing, limiting their applicability to pan-organ contrast translation.

Cardiac and region-specific benchmarks. Datasets such as ACDC [23] and MMWHS [24] offer high-quality cardiac MR/CT for segmentation and multi-modality analysis. Similarly, crossMoDA [22] focuses on inner-ear/temporal-bone MRI for domain adaptation. These are *task-focused and organ-specific* resources without systematic CE–NCE pairing, hence not tailored for generalizable contrast synthesis across diverse organs.

PET/CT and dose-constrained benchmarks. Whole-body PET/CT sets (e.g., FDG-PET/CT [25]) and ultra-low-dose PET studies [29] target cross-modality fusion or dose reduction and often assess PET synthesis from limited counts. While multi-

modality is present, CE–NCE pairing for CT/MR contrast translation is typically outside their scope.

Positioning of PMPBench. In contrast, PMPBench (*Paired-Contrast*) provides explicit per-patient CE–NCE pairing across 11 organs spanning both CT and MR. It is designed for multimodal translation and missing-modality synthesis, with harmonized preprocessing and radiologist-in-the-loop validation. As shown in Table I, most existing benchmarks emphasize either a single organ (e.g., brain, cardiac) or tasks orthogonal to contrast translation (e.g., PET dose reduction). PMPBench fills this gap by offering multi-organ breadth, dual-modality coverage, and rigorously verified CE–NCE pairs—enabling clinically meaningful benchmarking of contrast synthesis methods.

III. METHODOLOGY

A. Preliminary: Latent Flow Matching

Flow Matching (FM) [30], [31] learns a continuous transport map between two distributions over a data space $\mathcal{X} \subseteq \mathbb{R}^d$, using only samples and without access to likelihoods. Latent Flow Matching (LFM) [32], [33] extends FM by introducing a lower-dimensional latent space \mathcal{Z} . An encoder $E_\phi : \mathcal{X} \rightarrow \mathcal{Z}$ maps data into this latent space, where a transport map is learned, i.e. $\mathbf{z} := E_\phi(\mathbf{x})$.

Let π_0, π_1 be distributions over the latent space $\mathcal{Z} \subseteq \mathbb{R}^d$. Define a time-dependent velocity field $v : \mathcal{Z} \times [0, 1] \rightarrow \mathbb{R}^d$ and consider a stochastic process $(\mathbf{z}_t)_{t \in [0, 1]}$ governed by the stochastic differential equation (SDE):

$$d\mathbf{z}_t = v(\mathbf{z}_t, t)dt + \sigma(\mathbf{z}_t, t)dB_t, \quad \mathbf{z}_0 \sim \pi_0, \quad (2)$$

where B_t is standard Brownian motion and σ is the diffusion coefficient. In practice, v is approximated using the analytically defined target velocity field:

$$v^*(\mathbf{z}_t, t) := \frac{\mathbf{z}_1 - \mathbf{z}_t}{1 - t}, \quad (\mathbf{z}_0, \mathbf{z}_1) \sim \pi_0 \times \pi_1, \quad (3)$$

with intermediate states \mathbf{z}_t sampled from the stochastic interpolant (deterministic when $\sigma \rightarrow 0$):

$$\mathbf{z}_t = (1 - t)\mathbf{z}_0 + t\mathbf{z}_1 + \sigma\sqrt{t(1 - t)}\epsilon, \quad \epsilon \sim \mathcal{N}(0, I). \quad (4)$$

A neural velocity field $v_\theta(\mathbf{z}, t)$ is trained to match v^* by minimizing the following error:

$$\mathcal{L}_{\text{LFM}}(\theta) = \mathbb{E}_{t, \mathbf{z}_0, \mathbf{z}_1, \epsilon} \left[\left| v_\theta(\mathbf{z}_t, t) - \frac{\mathbf{z}_1 - \mathbf{z}_t}{1 - t} \right|^2 \right]. \quad (5)$$

Once trained, the learned velocity field v_θ is used to integrate the SDE in Eq. (2), transporting samples from \mathbf{z}_0 toward \mathbf{z}_1 . The final outputs in the original data space are obtained by decoding the transported latent samples: $\mathbf{x}_1 := D_\psi(\mathbf{z}_1)$.

B. FlowMI: Flow-based Missing Modality Imputation

Existing multimodal models often handle missing modalities by simply substituting zeros or noise, which yields semantically meaningless inputs and degrades performance.

In contrast, we propose **FlowMI**, which treats missing-modality imputation as a latent-space reconstruction problem.

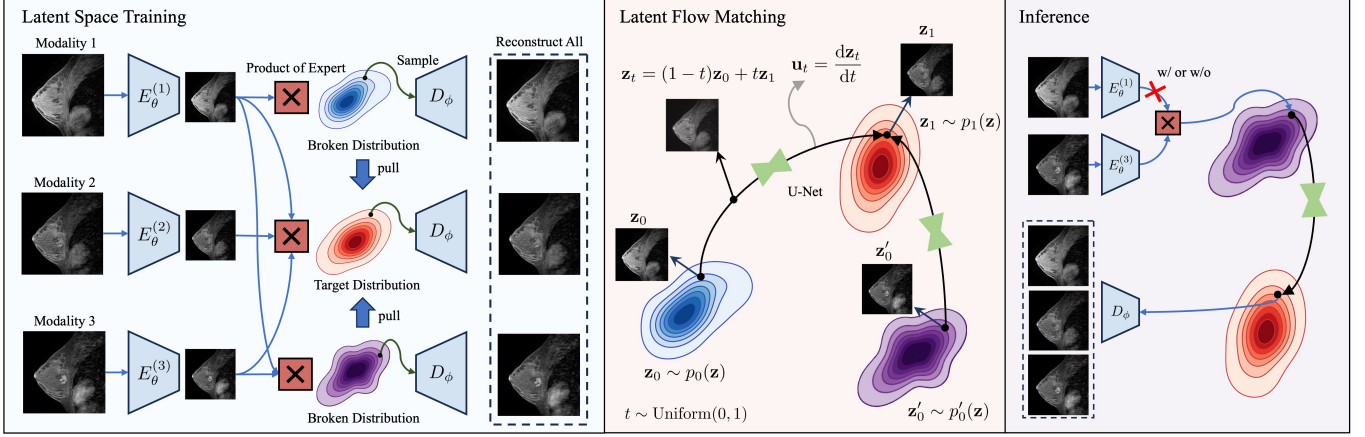


Fig. 3: Overview of the proposed FlowMI framework. **Left:** Modality-specific encoders $E_\theta^{(i)}$ map inputs into a latent space, which are fused via a product-of-experts. The distribution with all modalities defines the *target*, while cases with missing modalities define the *broken* distribution. **Middle:** Latent flow matching learns a smooth mapping from $p_0(z)$ (broken) to $p_1(z)$ (target) using a U-Net parameterization of the velocity field, $u_t = \frac{dz_t}{dt}$. **Right:** During inference, inputs with missing modalities are encoded and aligned through the learned flow, enabling consistent reconstruction or synthesis of complete modalities.

In our framework, a multi-modal autoencoder projects both complete and incomplete inputs into a shared latent space. An input with missing modalities produces a broken latent code (due to the absent information), and we learn a continuous flow in latent space to transform this broken code into a corresponding full latent code as if all modalities were present. We train this latent transformation via a flow-matching objective that aligns broken latents with their ground-truth complete counterparts, enabling accurate reconstruction under arbitrary missing patterns. We detail the components of FlowMI below.

Problem Setup. Consider a multi-modal input $\mathbf{x} = \{x^{(1)}, x^{(2)}, \dots, x^{(M)}\}$ consisting of M modalities. Due to data missingness, only a subset of these modalities may be available at inference time. We represent the observed pattern with a binary mask $\mathbf{m} \in \{0, 1\}^M$, where $\mathbf{m}^{(i)} = 1$ indicates modality i is present and $\mathbf{m}^{(i)} = 0$ indicates it is missing. Given a mask \mathbf{m} , let $\mathbf{x}^{\mathbf{m}}$ denote the set of observed modalities and $\mathbf{x}^{\neg\mathbf{m}}$ the set of missing modalities for input \mathbf{x} . The goal of imputation is to predict the missing components $\mathbf{x}^{\neg\mathbf{m}}$ from the observed ones $\mathbf{x}^{\mathbf{m}}$. For notational convenience, let $\mathbb{1} = \{1, 1, \dots, 1\}$ denote the mask of all ones (all modalities present), so $\mathbf{x}^{\mathbb{1}}$ is a fully observed input.

a) *Latent Representation.*: We adopt a multi-modal variational autoencoder (VAE) framework in which each modality has a dedicated encoder and all modalities share a common latent space. Formally, let $\mathcal{M} = \{1, 2, \dots, M\}$ be the set of modality indices. For each $m \in \mathcal{M}$, the encoder $E_\theta^{(m)}$ produces an approximate posterior distribution over the latent \mathbf{z} given that modality's input:

$$q_\theta^{(m)}(\mathbf{z} | \mathbf{x}^{(m)}) = E_\theta^{(m)}(\mathbf{x}^{(m)}). \quad (6)$$

When a subset of modalities $\mathcal{O} \subseteq \mathcal{M}$ is observed, we combine their encoders' outputs using a *Product-of-*

Experts (PoE) to obtain a unified latent posterior:

$$q_\theta(\mathbf{z} | \{\mathbf{x}^{(m)}\}_{m \in \mathcal{O}}) \propto p(\mathbf{z}) \prod_{m \in \mathcal{O}} q_\theta^{(m)}(\mathbf{z} | \mathbf{x}^{(m)}), \quad (7)$$

where $p(\mathbf{z})$ is the prior distribution (i.e. $\mathcal{N}(0, I)$). Missing modalities are handled by simply omitting their encoder “expert” from the product. A shared decoder D_ϕ then maps latent codes back to the data space. Given a latent sample \mathbf{z} drawn from the posterior q_θ , the decoder produces a reconstruction for all modalities: $\hat{\mathbf{x}} = D_\phi(\mathbf{z})$.

During training, we randomly mask out modalities to create partial observations and optimize three loss terms. Given an observed subset \mathcal{O} (with target modalities \mathcal{T} to reconstruct, typically $\mathcal{T} = \mathcal{M}$), we sample $\mathbf{z}_\mathcal{O} \sim q_\theta(\mathbf{z} | \mathbf{x}^{(m)} : m \in \mathcal{O})$ and decode it to $\hat{\mathbf{x}} = D_\phi(\mathbf{z}_\mathcal{O})$. We minimize the mean squared error between the reconstruction and the ground truth target $\mathbf{x}^{\mathbb{1}}$:

$$\mathcal{L}_{\text{rec}} = \mathbb{E}_{\mathbf{x}, \mathcal{O}} \left[\|D_\phi(\mathbf{z}_\mathcal{O}) - \mathbf{x}^{\mathbb{1}}\|_2^2 \right]. \quad (8)$$

To encourage coherence between partial-input latents and full-input latents, we introduce an alignment penalty that brings the two posterior distributions, the broken latent $\mathbf{z}^{\mathbf{m}}$ (from incomplete inputs) and the full latent $\mathbf{z}^{\mathbb{1}}$ (from complete inputs), closer. Using stop-gradient on $\mathbf{z}^{\mathbb{1}}$, we minimize:

$$\mathcal{L}_{\text{pull}} = \mathbb{E}_{\mathbf{x}, \mathbf{m}} \left[\|\mathbf{z}^{\mathbf{m}} - \text{sg}(\mathbf{z}^{\mathbb{1}})\|_2^2 \right], \quad (9)$$

where $\text{sg}(\cdot)$ denotes stop-gradient.

We also regularize each modality-specific latent distribution against the prior $p(\mathbf{z})$ (as in a standard VAE):

$$\mathcal{L}_{\text{KL}} = \sum_{m=1}^M \mathbb{E}_{\mathbf{x}^{(m)}} \left[D_{\text{KL}}(q_\theta^{(m)}(\mathbf{z}^{(m)} | \mathbf{x}^{(m)}) \| p(\mathbf{z})) \right]. \quad (10)$$

The full objective combines all three terms:

$$\mathcal{L} = \mathcal{L}_{\text{rec}} + \lambda \mathcal{L}_{\text{pull}} + \beta \mathcal{L}_{\text{KL}}, \quad (11)$$

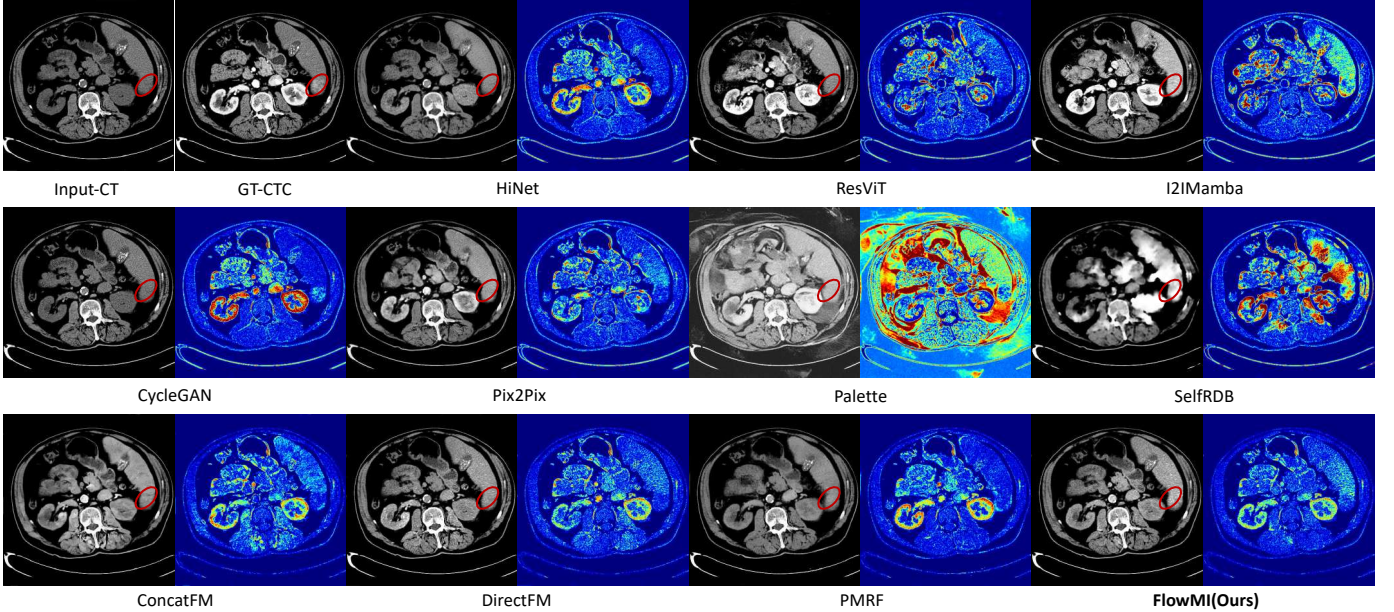


Fig. 4: CT \rightarrow CTC (liver). Red circles mark tumor regions. Input CT shows no clear lesion, ground-truth CTC shows bright enhancement. Most methods under-enhance the tumor, while ours recover the correct signal. Alongside each result, the blue residual maps visualize differences from ground truth (darker indicates larger error).

where λ and β control the relative contributions.

b) Latent Flow Matching.: The key component of FlowMI is a learned latent-space transformation that maps a broken latent code to its complete counterpart. We define a time-dependent vector field $v_\theta(\mathbf{z}, t)$ (implemented by a neural network) which generates a continuous trajectory from the broken latent to the full latent. Specifically, let $\mathbf{z}_0 = \mathbf{z}^m$ be the latent obtained from an incomplete input (with mask \mathbf{m}), and let $\mathbf{z}_1 = \mathbf{z}^1$ be the latent of the same input if all modalities were present. We define an ordinary differential equation (ODE) in latent space:

$$\frac{d\mathbf{z}_t}{dt} = v_\theta(\mathbf{z}_t, t), \quad \text{with } \mathbf{z}_0 := \mathbf{z}^m, \quad \text{and } \mathbf{z}_1 := \mathbf{z}^1, \quad (12)$$

To make learning the flow tractable, we prescribe a simple path and train v_θ to follow it. In particular, we use the straight-line interpolation between the endpoints as the target trajectory: $\mathbf{z}_t = (1 - t)\mathbf{z}_0 + t\mathbf{z}_1$. Along this path, the true velocity is constant and given by $d\mathbf{z}_t/dt = \mathbf{z}_1 - \mathbf{z}_0$. We train the vector field v_θ to match this velocity at every point along the path via a flow-matching loss:

$$\mathcal{L}_{LFM} = \mathbb{E}_{(\mathbf{z}_0, \mathbf{z}_1), t \sim \mathcal{U}(0, 1)} \left[\|v_\theta(\mathbf{z}_t, t) - (\mathbf{z}_1 - \mathbf{z}_0)\|^2 \right] \quad (13)$$

In essence, the learned flow function v_θ provides an efficient latent-space imputation dynamics that can handle arbitrary missing modality patterns.

c) Inference.: At test time, given an incomplete input \mathbf{x}^m with mask \mathbf{m} , we first obtain its broken latent code via the encoders: $\mathbf{z}^m = E_\theta(\mathbf{x}^m)$. We then apply the learned latent flow to transform \mathbf{z}^m toward an estimate of the full latent. Starting from $\mathbf{z}_0 = \mathbf{z}^m$, we numerically integrate the ODE

$d\mathbf{z}_t/dt = v_\theta(\mathbf{z}_t, t)$ from $t = 0$ to 1. For example, using a simple Euler integration with step size Δt , we update the latent as:

$$\hat{\mathbf{z}}_{t+\Delta t} = \mathbf{z}_t + \Delta t \cdot v_\theta(\mathbf{z}_t, t), \quad \text{for } t = 0, \Delta t, 2\Delta t, \dots, 1 - \Delta t. \quad (14)$$

After integrating to $t = 1$, we obtain an approximate full latent $\hat{\mathbf{z}}^1 = \mathbf{z}_1$. Finally, we feed this latent into the decoder to reconstruct the complete input: $\hat{\mathbf{x}}^1 = D_\phi(\hat{\mathbf{z}}^1)$. The output $\hat{\mathbf{x}}^1$ is the imputed multi-modal data, in which all originally missing modalities have been filled in by FlowMI.

IV. EXPERIMENTS

A. Baseline Setup

We evaluate and benchmark four categories of models for multimodal translation and missing-modality synthesis on PMPBench: **Direct methods** (UNet [39], ResViT (Transformer) [35], MambaIR [17], I2IMamba [4], and RestoreRWKV [40]); **GAN-based methods** (CycleGAN [10] and Pix2Pix [15]); **Diffusion-based methods** (PatchDiff (UNet) [12] and DiTSR (Transformer) [41]); **Flow-matching methods** (ConcatFM [37], DirectFM [37], PMRF [38], and our proposed FlowMI).

Training uses direct supervision on explicitly paired CE-NCCE scans. All methods are trained under the same data split and preprocessing pipeline (Sec. II-B), without external data. We follow each method’s public implementation. Training is performed on 2D slices from registered volumes, resized to a fixed resolution.

We report results using Peak Signal-to-Noise Ratio (PSNR), Structural Similarity Index Measure (SSIM), Kernel Inception Distance (KID), Fréchet Inception Distance (FID), and

TABLE II: Quantitative comparison on the PMPBench CT and MR paired pan-cancer contrast media dataset. Methods are grouped by generative mechanism and architecture. PSNR (dB) and SSIM (%) are reported as Mean±Standard Deviation. *Trans: Transformer.

Mechanism	Architecture	Methods	CT → CTC PSNR↑ SSIM(%)↑	DCE ₁ → DCE ₂ PSNR↑ SSIM(%)↑	DCE ₁ → DCE _{2,3} PSNR↑ SSIM(%)↑	DCE _{1,3} → DCE ₂ PSNR↑ SSIM(%)↑
Direct	UNet	HiNet [34]	22.23 ± 3.70 77.7 ± 10.3	23.41 ± 3.48 68.1 ± 11.9	23.88 ± 3.37 72.9 ± 8.32	26.47 ± 3.32 70.2 ± 12.2
	Trans	ResViT [35]	20.80 ± 3.11 74.2 ± 10.2	25.12 ± 3.16 70.5 ± 10.5	24.65 ± 2.81 63.5 ± 10.8	25.24 ± 2.89 59.8 ± 15.0
	Mamba	I2IMamba [4]	20.97 ± 3.20 74.6 ± 10.3	23.25 ± 2.37 55.9 ± 14.5	23.57 ± 2.50 58.0 ± 13.0	26.82 ± 3.32 70.1 ± 11.8
GAN	UNet	CycleGAN [10]	21.90 ± 3.98 75.8 ± 13.2	24.18 ± 3.33 65.7 ± 13.3	24.46 ± 3.52 71.4 ± 12.0	25.74 ± 3.28 72.4 ± 12.2
	UNet	Pix2Pix [15]	21.39 ± 3.10 72.6 ± 13.8	23.24 ± 3.35 64.6 ± 14.3	23.90 ± 2.97 72.2 ± 8.95	26.42 ± 3.10 70.2 ± 10.4
Diffusion	UNet	Palette [16]	15.88 ± 5.30 33.2 ± 21.8	9.54 ± 2.17 9.7 ± 6.38	10.19 ± 1.99 14.5 ± 6.16	4.79 ± 1.25 5.47 ± 2.55
	UNet	SelfRDB [36]	17.16 ± 2.38 72.5 ± 7.90	23.40 ± 3.31 57.6 ± 16.4	24.98 ± 2.87 67.6 ± 13.5	26.66 ± 3.79 70.2 ± 11.9
Flow-matching	UNet	ConcatFM [37]	23.10 ± 4.12 77.1 ± 9.28	26.31 ± 2.67 72.9 ± 6.61	26.25 ± 2.49 71.8 ± 6.18	29.06 ± 2.73 76.1 ± 6.63
	UNet	DirectFM [37]	22.84 ± 3.88 76.7 ± 11.4	25.74 ± 3.14 68.5 ± 8.09	25.98 ± 3.05 71.1 ± 8.22	27.90 ± 3.18 74.2 ± 7.69
	UNet	PMRF [38]	21.91 ± 3.95 76.6 ± 11.6	25.06 ± 3.60 67.5 ± 8.28	26.11 ± 3.80 70.1 ± 8.32	27.53 ± 4.25 74.9 ± 5.31
	UNet	FlowMI (Ours)	24.47 ± 4.15 78.5 ± 8.62	26.52 ± 3.13 74.2 ± 9.33	26.63 ± 3.11 73.7 ± 8.06	29.17 ± 3.24 76.2 ± 7.65

Learned Perceptual Image Patch Similarity (LPIPS) as quantitative metrics.

B. Implementation Details

Here we provide the training and inference configuration of FlowMI, including model architecture, optimization settings, and implementation details.

Model Architecture. FlowMI is implemented as a 3D latent flow matching framework that operates directly in the latent space of a 3D variational autoencoder (VAE). The VAE adopts a 3D U-Net backbone with a depth of 4, residual blocks at each stage, and group normalization, producing a latent representation with 256 channels. The flow-matching module uses a similarly structured 3D U-Net to predict the continuous velocity field that transports latents.

Training Configuration. All models are trained using AdamW optimizer with a learning rate of 1×10^{-4} . A cosine annealing schedule with linear warm-up for the first 5% of training steps is applied. Due to the high memory cost of 3D volumes, the batch size is set to 2 per GPU with gradient accumulation to achieve an effective batch size of 8. We train for 200 epochs on all settings unless otherwise specified. To stabilize flow learning, we follow standard continuous-time flow matching and uniformly sample time steps $t \sim \mathcal{U}(0, 1)$ during training. Experiments are conducted on NVIDIA A6000 GPUs.

C. Experiment Results

Quantitative comparison. table II and table III show that flow-matching methods consistently outperform direct, GAN, and diffusion baselines. Across all tasks, our model achieves the highest PSNR, SSIM and SSIM, LPIPS, FID and KID, with a clear lead on CT→CTC, demonstrating its ability to generate both sharp and structurally faithful reconstructions. We observe that $n \rightarrow 1$ translation generally benefits from complementary temporal information, whereas $1 \rightarrow n$ remains the most challenging due to the difficulty of preserving structural consistency across multiple targets. The variances capture the strong heterogeneity of PMPBench, which spans

11 organs and multiple contrast modalities, thereby increasing the learning difficulty for cross-modality translation. Overall, flow-matching achieves consistently high performance with smaller variance, indicating enhanced stability and generalization across diverse conditions.

Qualitative comparison. As shown in fig. 4, the qualitative results echo the quantitative findings. While most methods generate visually plausible CT images, they often leave tumor regions under-enhanced, making lesions difficult to distinguish. In contrast, our model successfully reproduces the bright enhancement seen in the ground-truth CTC, and the accompanying blue residual maps confirm lower reconstruction errors. These results highlight that beyond visual realism, clinically accurate contrast synthesis is essential for downstream diagnosis.

V. ETHICS AND DATA AVAILABILITY

We verified the licenses and acquisition procedures of all resources to ensure redistribution compliance. Dataset access is provided upon submission of an agreement form and approval from the original data sources. It will be released on our project website under a CC BY-NC-ND 4.0 license, prohibiting private redistribution. All users must obtain permission through the website before downloading.

VI. CONCLUSION

In this work, we introduced PMPBench, a comprehensive pan-cancer benchmark for multimodal image translation and missing-modality synthesis in clinically realistic settings. It provides high-quality, per-patient paired CT and MR scans across 11 organs with both contrast-enhanced and non-contrast modalities, curated through a standardized and reproducible pipeline. We defined three benchmark tasks and reported reference results using representative generative models. While limitations remain, such as biases in public data sources and variability in clinical imaging, PMPBench offers a foundation for developing robust multimodal translation methods and advancing clinically reliable decision support. Future work could extend the dataset with additional modalities, larger

TABLE III: LPIPS, FID, and KID comparison across methods on PMPBench.

Mechanism	Architecture	Methods	CT → CTC			DCE ₁ → DCE ₂			DCE ₁ → DCE _{2,3}			DCE _{1,3} → DCE ₂		
			LPIPS↓	FID↓	KID↓	LPIPS↓	FID↓	KID↓	LPIPS↓	FID↓	KID↓	LPIPS↓	FID↓	KID↓
Direct	UNet	HiNet [34]	0.084	0.01	14.62	0.181	0.02	37.68	0.163	0.01	30.63	0.113	0.01	18.83
	Trans	ResViT [35]	0.109	0.01	17.53	0.224	0.02	43.18	0.146	0.01	18.31	0.142	0.01	31.08
	Mamba	I2IMamba [4]	0.099	0.00	12.21	0.217	0.02	40.17	0.181	0.01	28.88	0.099	0.00	12.21
GAN	UNet	CycleGAN [10]	0.079	0.00	8.98	0.150	0.01	20.88	0.159	0.01	22.25	0.114	0.01	21.40
	UNet	Pix2Pix [15]	0.109	0.01	22.70	0.218	0.02	48.92	0.186	0.01	36.21	0.127	0.01	32.88
Diffusion	UNet	Palette [16]	0.216	0.03	41.19	0.755	0.32	270.9	0.747	0.29	255.7	0.929	0.52	412.3
	UNet	SelfRDB [36]	0.189	0.07	78.80	0.254	0.03	53.98	0.203	0.03	50.24	0.186	0.02	37.30
Flow-matching	UNet	ConcatFM [37]	0.080	0.01	18.47	0.137	0.01	19.18	0.128	0.02	18.44	0.109	0.02	20.67
	UNet	DirectFM [37]	0.074	0.01	15.08	0.214	0.03	26.74	0.201	0.03	28.83	0.169	0.02	26.41
	UNet	PMRF [38]	0.090	0.02	24.74	0.212	0.02	28.37	0.149	0.02	22.64	0.214	0.02	22.18
	UNet	FlowMI (Ours)	0.065	0.01	11.55	0.120	0.01	16.74	0.101	0.01	14.63	0.090	0.01	12.85

cohorts, and more advanced synthesis techniques to further enhance generalization and applicability.

APPENDIX

Here we provide extended statistics for PMPBench as well as the original data sources of each collection.

All scans were obtained by downloading raw DICOM or NIfTI files from publicly available repositories. The included collections are: Adrenal-ACC-Ki67-Seg [42] TCGA-OV [43], TCGA-UCEC [44], CPTAC-UCEC [45], TCGA-STAD [46], CPTAC-PDA [47], HCC-TACE-Seg [48], TCGA-LIHC [49], CMB-CRC [50], TCGA-COAD [51], TCGA-BLCA [52], TCGA-KIRC [53], C4KC-KiTS [54], CPTAC-CCRCC [55], TCGA-KIRP [56], TCGA-KICH [57], CMB-LCA [58], CPTAC-LSCC [59], CPTAC-LUAD [60], Lung-PET-CT-Dx [61], TCGA-LUSC [62], Anti-PD-1_Lung [63], TCGA-BRCA [64] [65], UCSF [66] [67] [65], I-SPY 1 [68] [65].

Registration was implemented via the 3D Slicer Elastix extension using ITK-Elastix backend. The rigid and affine stages used Advanced Mattes Mutual Information (32 bins), a 4-level resolution pyramid (shrink factors [8,4,2,1]), and adaptive stochastic gradient descent optimization. The deformable stage employed a third-order B-spline transform (FinalGridSpacingInVoxels = 10) with 3 resolution levels and up to 2000 iterations per level. All registrations were visually inspected for anatomical consistency before inclusion.

We performed rigid and affine alignment between CE and NCE scans using the **3D Slicer** Elastix module, followed by deformable registration for motion-prone organs (e.g., liver, lung). All stages used the ITK-elastix backend with the following representative settings: **rigid** (Euler3DTransform) and **affine** (AffineTransform) stages employed the Advanced Mattes Mutual Information (32 bins) as the similarity metric, a multi-resolution pyramid with 4 levels (shrink factors [8, 4, 2, 1]; smoothing sigmas [3, 2, 1, 0] vox), the Adaptive Stochastic Gradient Descent optimizer (max 1024 iterations per level), and linear interpolation for resampling;

the **deformable** stage used a third-order B-spline transform (BSpline order = 3) with 3 resolution levels (shrink factors [4, 2, 1]; smoothing sigmas [2, 1, 0] vox), max 2000 iterations per level, and a final control-point spacing of 10 voxels (FinalGridSpacingInVoxels= 10), while final resampling used B-spline interpolation. This configuration achieved accurate anatomical correspondence while maintaining computational efficiency, reducing potential supervision bias due to CE/NCE misalignment.

REFERENCES

- [1] Martin Heusel, Hubert Ramsauer, Thomas Unterthiner, Bernhard Nessler, and Sepp Hochreiter, “Gans trained by a two time-scale update rule converge to a local nash equilibrium,” *Advances in neural information processing systems*, vol. 30, 2017.
- [2] Robin Rombach, Andreas Blattmann, Dominik Lorenz, Patrick Esser, and Björn Ommer, “High-resolution image synthesis with latent diffusion models,” in *Proceedings of the IEEE/CVF conference on computer vision and pattern recognition*, 2022, pp. 10684–10695.
- [3] William Peebles and Saining Xie, “Scalable diffusion models with transformers,” in *ICCV*, 2023, pp. 4195–4205.
- [4] Omer F Atli, Bilal Kabas, Fuat Arslan, Arda C Demirtas, Mahmut Yurt, Onat Dalmaz, and Tolga Cukur, “I2i-mamba: Multi-modal medical image synthesis via selective state space modeling,” *arXiv preprint arXiv:2405.14022*, 2024.
- [5] Agisilaos Chartsias, Thomas Joyce, Mario Valerio Giuffrida, and Sotirios A. Tsaftaris, “Multimodal mr synthesis via modality-invariant latent representation,” *IEEE Transactions on Medical Imaging*, vol. 37, pp. 803–814, 3 2018.
- [6] Maria Correia de Verdier, Rachit Saluja, Louis Gagnon, Dominic LaBella, Ujjwal Baid, Nourel Hoda Tahon, Martha Folty-Dumitru, Jikai Zhang, Maram Alafif, Saif Baig, et al., “The 2024 brain tumor segmentation (brats) challenge: Glioma segmentation on post-treatment mri,” *arXiv preprint arXiv:2405.18368*, 2024, <https://arxiv.org/abs/2405.18368>.
- [7] Yuanfeng Ji, Haotian Bai, Chongjian Ge, Jie Yang, Ye Zhu, Ruimao Zhang, Zhen Li, Lingyan Zhang, Wanling Ma, Xiang Wan, et al., “Amos: A large-scale abdominal multi-organ benchmark for versatile medical image segmentation,” *Advances in neural information processing systems*, vol. 35, pp. 36722–36732, 2022.
- [8] Kenneth Clark, Bruce Vendt, Kirk Smith, John Freymann, Justin Kirby, Paul Koppel, Stephen Moore, Stanley Phillips, David Maffitt, Michael Pringle, Lawrence Tarbox, and Fred Prior, “The cancer imaging archive (tcia): maintaining and operating a public information repository,” 2013, TCIA website: <https://www.cancerimagingarchive.net/>.
- [9] Blaine Rister, Darvin Yi, Kaushik Shivakumar, Tomomi Nobashi, and Daniel L Rubin, “Ct-org, a new dataset for multiple organ segmentation in computed tomography,” *Scientific Data*, vol. 7, no. 1, pp. 381, 2020.

TABLE IV: Detailed statistics of the PMPBench dataset.

Modality	Overall of Modality	System	Overall of Dataset	Organ	Overall of Organ	Source Dataset	Overall of Dataset	Overall of Organ	License	
MR	1116	Female Reproductive	1116	Breast	1116	TCGA-BRCA UCSF I-SPY 1	378 180 558	Breast Cancer	CC BY 3.0 CC BY 3.0 CC BY 3.0	
CT	1526	Endocrine	82	Adrenal	82	Adrenal-ACC-Ki67-Seg	82	Adrenocortical carcinoma	CC BY 4.0	
				Ovary	12	TCGA-OV	12	Ovarian Serous Cystadenocarcinoma	CC BY 3.0	
		Female Reproductive		Uterus	54	TCGA-UCEC	14	Uterine Corpus Endometrial Carcinoma	CC BY 3.0	
				Stomach	86	CPTAC-UCEC	40	Uterine Corpus Endometrial Carcinoma	CC BY 3.0	
		Digestive	614	Pancreas	54	CPTAC-PDA	54	Ductal Adenocarcinoma	CC BY 3.0	
				Liver	432	HCC-TACE-Seg	360	Hepatocellular carcinoma	CC BY 3.0	
				Colon	22	TCGA-LIHC	72	Hepatocellular carcinoma	CC BY 3.0	
				Bladder	86	CMB-CRC	18	Colorectal Cancer	CC BY 3.0	
		Urinary	684	Kidney	598	TCGA-COAD	4	Colon adenocarcinoma	CC BY 3.0	
				TCGA-BLCA	86	TCGA-KIRC	278	Bladder Endothelial Carcinoma	CC BY 3.0	
				C4KC-KiTS	216	CPTAC-CCRCC	66	Kidney Renal Clear Cell Carcinoma	CC BY 3.0	
				TCGA-KIRP	26	TCGA-KIRP	26	Kidney Cancer	CC BY 3.0	
		Respiratory	80	Lung	80	TCGA-KICH	12	Clear Cell Carcinoma	CC BY 3.0	
				CMB-LCA	28	Lung-PET-CT-Dx	28	Kidney Renal Papillary Cell Carcinoma	CC BY 3.0	
				Anti-PD-1_Lung	6	Anti-PD-1_Lung	6	Kidney Chromophobe	CC BY 3.0	
				TCGA-LUSC	2	TCGA-LUSC	2	Lung Cancer	CC BY 4.0	
				CPTAC-LSCC	28	CPTAC-LSCC	28	Lung Cancer	CC BY 4.0	
				CPTAC-LUAD	10	CPTAC-LUAD	10	Lung Squamous Cell Carcinoma	CC BY 3.0	
								Squamous Cell Carcinoma	CC BY 3.0	
								Lung Adenocarcinoma	CC BY 3.0	

[10] Jun-Yan Zhu, Taesung Park, Phillip Isola, and Alexei A Efros, “Unpaired image-to-image translation using cycle-consistent adversarial networks,” in *Proceedings of the IEEE international conference on computer vision*, 2017, pp. 2223–2232.

[11] Guangkai Xu, Yongtao Ge, Mingyu Liu, Chengxiang Fan, Kangyang Xie, Zhiyue Zhao, Hao Chen, and Chunhua Shen, “Diffusion models trained with large data are transferable visual models,” *arXiv e-prints*, pp. arXiv-2403, 2024.

[12] Ozan Özdenizci and Robert Legenstein, “Restoring vision in adverse weather conditions with patch-based denoising diffusion models,” *IEEE TPAMI*, vol. 45, no. 8, pp. 10346–10357, 2023.

[13] Yaron Lipman, Ricky TQ Chen, Heli Ben-Hamu, Maximilian Nickel, and Matt Le, “Flow matching for generative modeling,” *arXiv preprint arXiv:2210.02747*, 2022.

[14] Hao Chen, Rui Yin, Yifan Chen, Qi Chen, and Chao Li, “Learning patient-specific disease dynamics with latent flow matching for longitudinal imaging generation,” *arXiv preprint arXiv:2512.09185*, 2025.

[15] Phillip Isola, Jun-Yan Zhu, Tinghui Zhou, and Alexei A Efros, “Image-to-image translation with conditional adversarial networks,” in *Proceedings of the IEEE conference on computer vision and pattern recognition*, 2017, pp. 1125–1134.

[16] Chitwan Saharia, William Chan, Huiwen Chang, Chris Lee, Jonathan Ho, Tim Salimans, David Fleet, and Mohammad Norouzi, “Palette: Image-to-image diffusion models,” in *ACM SIGGRAPH 2022 conference proceedings*, 2022, pp. 1–10.

[17] Hang Guo, Jinmin Li, Tao Dai, Zhihao Ouyang, Xudong Ren, and Shu-Tao Xia, “Mambair: A simple baseline for image restoration with state-space model,” in *European conference on computer vision*. Springer, 2024, pp. 222–241.

[18] Stefan Klein, Margreet Staring, Koen Murphy, and et al., “elastix: a toolbox for intensity-based medical image registration,” *IEEE Transactions on Medical Imaging*, vol. 29, no. 1, pp. 196–205, 2010.

[19] Vanya V Valindria, Nick Pawlowski, Martin Rajchl, Ioannis Lavdas, Eric O Aboagye, Andrea G Rockall, Daniel Rueckert, and Ben Glocker, “Multi-modal learning from unpaired images: Application to multi-organ segmentation in ct and mri,” in *2018 IEEE winter conference on applications of computer vision (WACV)*. IEEE, 2018, pp. 547–556, .

[20] Nazanin Maleki, Raisa Amiruddin, Ahmed W Moawad, Nikolay Yordanov, Athanasios Gkampenis, Pascal Fehringer, Fabian Umeh, Crystal Chukwurah, Fatima Memon, Bojan Petrovic, et al., “Analysis of the miccai brain tumor segmentation–metastases (brats-mets) 2025 lighthouse challenge: Brain metastasis segmentation on pre-and post-treatment mri,” *arXiv preprint arXiv:2504.12527*, 2025.

[21] “Ixi dataset (rrid:scr_005839),” <http://brain-development.org/ixi-dataset/>.

[22] Reuben Dorent, Aaron Kujawa, Marina Ivory, Spyridon Bakas, Nicola Rieke, Samuel Joutard, Ben Glocker, Jorge Cardoso, Marc Modat, Kayhan Batmanghelich, et al., “Crossmoda 2021 challenge: Benchmark of cross-modality domain adaptation techniques for vestibular schwannoma and cochlea segmentation,” *Medical Image Analysis*, vol. 83, pp. 102628, 2023, <https://www.sciencedirect.com/science/article/pii/S1361841522002560>.

[23] Olivier Bernard, Alain Lalande, Clement Zotti, Frederick Cervenansky, Xin Yang, Pheng-Ann Heng, Irem Cetin, Karim Lekadir, Oscar Camara,

Miguel Angel Gonzalez Ballester, et al., "Deep learning techniques for automatic mri cardiac multi-structures segmentation and diagnosis: is the problem solved?," *IEEE transactions on medical imaging*, vol. 37, no. 11, pp. 2514–2525, 2018, <https://ieeexplore.ieee.org/document/8360453>.

[24] Xiahai Zhuang, "Multivariate mixture model for myocardial segmentation combining multi-source images," *IEEE transactions on pattern analysis and machine intelligence*, vol. 41, no. 12, pp. 2933–2946, 2018, <https://ieeexplore.ieee.org/abstract/document/8458220>.

[25] Sergios Gatidis, Tobias Hepp, Marcel Früh, Christian La Fougère, Konstantin Nikolaou, Christina Pfannenberg, Bernhard Schölkopf, Thomas Küstner, Clemens Cyran, and Daniel Rubin, "A whole-body fdg-pet/ct dataset with manually annotated tumor lesions," *Scientific Data*, vol. 9, no. 1, pp. 601, 2022, <https://www.scopus.com/pages/publications/85139504476>.

[26] Hongwei Bran Li, Gian Marco Conte, Qingqiao Hu, Syed Muhammad Anwar, Florian Kofler, Ivan Ezhov, Koen van Leemput, Marie Piraud, Maria Diaz, Byrne Cole, et al., "The brain tumor segmentation (brats) challenge 2023: Brain mr image synthesis for tumor segmentation (bratsyn)," *ArXiv*, pp. arXiv–2305, 2024, <https://PMC10441440/>.

[27] Pamela J LaMontagne, Tammie LS Benzinger, John C Morris, Sarah Keefe, Russ Hornbeck, Chengjie Xiong, Elizabeth Grant, Jason Hassenstab, Krista Moulder, Andrei G Vlassenko, et al., "Oasis-3: longitudinal neuroimaging, clinical, and cognitive dataset for normal aging and alzheimer disease," *medrxiv*, pp. 2019–12, 2019, <https://www.medrxiv.org/content/10.1101/2019.12.13.19014902v1>.

[28] Mónica Rivera Mindt, Alyssa Arentoft, Amanda T Calcetas, Vanessa A Guzman, Hannatu Amaza, Adeyinka Ajayi, Miriam T Ashford, Omobolanle Ayo, Lisa L Barnes, Alicia Camuy, et al., "The alzheimer's disease neuroimaging initiative-4 (adni-4) engagement core: A culturally informed, community-engaged research (ci-er) model to advance brain health equity," *Alzheimer's & Dementia*, vol. 20, no. 12, pp. 8279–8293, 2024, <https://alz-journals.onlinelibrary.wiley.com/doi/full/10.1002/alz.14242>.

[29] "Ultra-low dose pet imaging challenge 2024 (udpet)," Dataset and challenge information available online, 2024, Accessed via <https://udpet-challenge.github.io/>.

[30] Yaron Lipman, Ricky TQ Chen, Heli Ben-Hamu, Maximilian Nickel, and Matthew Le, "Flow matching for generative modeling," in *The Eleventh International Conference on Learning Representations*, 2023.

[31] Xingchao Liu, Chengyue Gong, et al., "Flow straight and fast: Learning to generate and transfer data with rectified flow," in *The Eleventh International Conference on Learning Representations*, 2022.

[32] Quan Dao, Hao Phung, Binh Nguyen, and Anh Tran, "Flow matching in latent space," *arXiv preprint arXiv:2307.08698*, 2023.

[33] Clément Chadebec, Onur Tasar, Sanjeev Sreetharan, and Benjamin Aubin, "Lbm: Latent bridge matching for fast image-to-image translation," *arXiv preprint arXiv:2503.07535*, 2025.

[34] Tao Zhou, Huazhu Fu, Geng Chen, Jianbing Shen, and Ling Shao, "Hinet: hybrid-fusion network for multi-modal mr image synthesis," *IEEE transactions on medical imaging*, vol. 39, no. 9, pp. 2772–2781, 2020.

[35] Onat Dalmaz, Mahmut Yurt, and Tolga Çukur, "Resvit: Residual vision transformers for multimodal medical image synthesis," *IEEE Transactions on Medical Imaging*, vol. 41, no. 10, pp. 2598–2614, 2022.

[36] Fuat Arslan, Bilal Kabas, Onat Dalmaz, Muzaffer Ozbeý, and Tolga Çukur, "Self-consistent recursive diffusion bridge for medical image translation," *Medical Image Analysis*, vol. 106, pp. 103747, 2025.

[37] Yaron Lipman, Ricky TQ Chen, Heli Ben-Hamu, Maximilian Nickel, and Matt Le, "Flow matching for generative modeling," *arXiv preprint arXiv:2210.02747*, 2022.

[38] Guy Ohayon, Tomer Michaeli, and Michael Elad, "Posterior-mean rectified flow: Towards minimum mse photo-realistic image restoration," *arXiv preprint arXiv:2410.00418*, 2024.

[39] Olaf Ronneberger, Philipp Fischer, and Thomas Brox, "U-net: Convolutional networks for biomedical image segmentation," in *Medical image computing and computer-assisted intervention–MICCAI 2015: 18th international conference, Munich, Germany, October 5–9, 2015, proceedings, part III 18*. Springer, 2015, pp. 234–241.

[40] Zhiwen Yang, Jiayin Li, Hui Zhang, Dan Zhao, Bingzheng Wei, and Yan Xu, "Restore-rwkv: Efficient and effective medical image restoration with rwkv," 2024.

[41] Kun Cheng, Lei Yu, Zhijun Tu, Xiao He, Liyu Chen, Yong Guo, Mingrui Zhu, Nannan Wang, Xinbo Gao, and Jie Hu, "Effective diffusion transformer architecture for image super-resolution," in *Proceedings of the AAAI Conference on Artificial Intelligence*, 2025, pp. 2455–2463.

[42] Ahmed W Moawad, Ayahallah A Ahmed, Mohab Elmohr, Mohamed Eltaher, Mohammed Amir Habra, Sarah Fisher, Nancy Perrier, Miao Zhang, David Fuentes, and Khaled Elsayes, "Voxel-level segmentation of pathologically-proven adrenocortical carcinoma with ki-67 expression (adrenal-acc-ki67-seg)[data set]," *The Cancer Imaging Archive*, vol. 8, 2023.

[43] Chandra Holback, Rose Jarosz, Fred Prior, David G Mutch, Priya Bhosale, Kimberly Garcia, Yueh Lee, Shanah Kirk, Cheryl A Sadow, Seth Levine, et al., "The cancer genome atlas ovarian cancer collection (tcga-ov)(version 4)[data set]," *The Cancer Imaging Archive*, vol. 10, pp. K9, 2016.

[44] BJ Erickson, D Mutch, L Lippmann, and R Jarosz, "The cancer genome atlas uterine corpus endometrial carcinoma collection (tcga-ucec)," *The Cancer Imaging Archive*, 2016.

[45] National Cancer Institute Clinical Proteomic Tumor Analysis Consortium et al., "The clinical proteomic tumor analysis consortium uterine corpus endometrial carcinoma collection (cptac-ucec), version 10 [dataset]," *The Cancer Imaging Archive*, vol. 10, pp. k9, 2019.

[46] FR Lucchesi and ND Aredeas, "The cancer genome atlas stomach adenocarcinoma collection (tcga-stad)," *The Cancer Imaging Archive*, 2016.

[47] National Cancer Institute Clinical Proteomic Tumor Analysis Consortium (CPTAC), "The clinical proteomic tumor analysis consortium pancreatic ductal adenocarcinoma collection (cptac-pda) (version 15) [data set]," 2018, The Cancer Imaging Archive. <https://doi.org/10.7937/k9/cia.2018.sc20fo18>.

[48] AW Moawad, D Fuentes, A Morshid, AM Khalaf, MM Elmohr, A Abu-saif, JD Hazle, AO Kaseb, M Hassan, A Mahvash, et al., "Multimodality annotated hcc cases with and without advanced imaging segmentation," *The Cancer Imaging Archive (TCIA)*, 2021.

[49] Bradley J Erickson, Shanah Kirk, Y Lee, Oliver Bathe, Melissa Kearns, C Gerdes, Kimberly Rieger-Christ, and John Lemmerman, "The cancer genome atlas liver hepatocellular carcinoma collection (tcga-lihc)(version 5)[data set]," *The Cancer Imaging Archive*, 2016.

[50] Cancer Moonshot Biobank, "Cancer moonshot biobank – colorectal cancer collection (cmb-crc) (version 8) [data set]," 2022, The Cancer Imaging Archive. <https://doi.org/10.7937/djg7-gz87>.

[51] S Kirk, Y Lee, CA Sadow, S Levine, C Roche, E Bonaccio, and J Filippini, "The cancer genome atlas colon adenocarcinoma collection (tcga-coad)(version 3)[data set]," *The Cancer Imaging Archive*. <https://doi.org/10.7937/k9/cia.2016.16>.

[52] Shanah Kirk, Yueh Lee, Fabiano R Lucchesi, Natalia D Aredeas, Nicholas Gruszauskas, James Catto, Kimberly Garcia, Rose Jarosz, Vinay Duddalwar, Bino Varghese, et al., "The cancer genome atlas urothelial bladder carcinoma collection (tcga-blca)," in *The Cancer Imaging Archive*. 2016.

[53] Oguz Akin, Pierre Elnajjar, Matthew Heller, Rose Jarosz, Bradley J Erickson, Shanah Kirk, Yueh Lee, Marston W Linehan, Rabindra Gautam, Raghu Vikram, et al., "The cancer genome atlas kidney renal clear cell carcinoma collection (tcga-kirc)(version 3)[data set]," *Cancer Imaging Arch*, 2016.

[54] Nicholas Heller, Nitlesh Sathianathan, Arveen Kalapara, Ethan Walczak, Kenneth Moore, Holly Kaluzniak, Jacob Rosenberg, Paul Blake, Zachary Rengel, Michael Oestreich, Joel Dean, Matthew Tradewell, Adeel Shah, Rishi Tejpaul, Zachary Edgerton, Matthew Peterson, Sohaib Raza, Samip Regmi, Nikolaos Papanikolopoulos, and Christopher Weight, "Data from c4kc-kits [data set]," 2019, The Cancer Imaging Archive. <https://doi.org/10.7937/TCIA.2019.IX49E8NX>.

[55] National Cancer Institute Clinical Proteomic Tumor Analysis Consortium (CPTAC), "The clinical proteomic tumor analysis consortium clear cell renal cell carcinoma collection (cptac-cercc) (version 14) [data set]," 2018, The Cancer Imaging Archive. <https://doi.org/10.7937/k9/cia.2018.oblann27>.

[56] Marston Linehan, R Gautam, S Kirk, Y Lee, C Roche, E Bonaccio, J Filippini, K Rieger-Christ, J Lemmerman, and R Jarosz, "The cancer genome atlas cervical kidney renal papillary cell carcinoma collection (tcga-kirp), version 4," *The Cancer Imaging Archive*, 2016.

[57] M Linehan, R Gautam, C Sadow, and SJ Levine, "The cancer genome atlas kidney chromophobe collection (tcga-kich)(version 3)," *The Cancer Imaging Archive*, 2016.

[58] C Biobank, "Cancer moonshot biobank-lung cancer collection (cmb-lca)(version 3)[dataset]," *The Cancer Imaging Archive*, 2022.

[59] National Cancer Institute Clinical Proteomic Tumor Analysis Consortium et al., “The clinical proteomic tumor analysis consortium lung squamous cell carcinoma collection (cptac-lscc),” (*No Title*), 2018.

[60] National Cancer Institute Clinical Proteomic Tumor Analysis Consortium et al., “The clinical proteomic tumor analysis consortium lung adenocarcinoma collection (cptac-luad)(version 12)[data set],” *The Cancer Imaging Archive. Published online*, 2018.

[61] Peng Li, Shaoke Wang, Tianyu Li, Jie Lu, Yufan HuangFu, and Dong Wei Wang, “A large-scale ct and pet/ct dataset for lung cancer diagnosis (lung-pet-ct-dx) [data set],” 2020, The Cancer Imaging Archive. <https://doi.org/10.7937/TCIA.2020.NNC2-0461>.

[62] S Kirk, Y Lee, P Kumar, J Filippini, B Albertina, M Watson, K Rieger-Christ, and J Lemmerman, “The cancer genome atlas lung squamous cell carcinoma collection (tcga-lusc)(version 4)[data set],” *The Cancer Imaging Archive*, 2016.

[63] Pranathi Madhavi, Shweta Patel, and Anne S. Tsao, “Data from anti-pd-1 immunotherapy lung [data set],” 2019, The Cancer Imaging Archive. <https://doi.org/10.7937/tcia.2019.zjjwb9ip>.

[64] Wilma Lingle, Bradley J Erickson, Margarita L Zuley, Rose Jarosz, Ermelinda Bonaccio, Joe Filippini, Jose M Net, Len Levi, Elizabeth A Morris, Gloria G Figler, et al., “The cancer genome atlas breast invasive carcinoma collection (tcga-breca),” (*No Title*), 2016.

[65] Jia Wu, Chao Li, Michael Gensheimer, Sukhmani Padda, Fumi Kato, Hiroki Shirato, Yiran Wei, Carola-Bibiane Schönlieb, Stephen John Price, David Jaffray, et al., “Radiological tumour classification across imaging modality and histology,” *Nature machine intelligence*, vol. 3, no. 9, pp. 787–798, 2021.

[66] Ka-Loh Li, Savannah C Partridge, Bonnie N Joe, Jessica E Gibbs, Ying Lu, Laura J Esserman, and Nola M Hylton, “Invasive breast cancer: predicting disease recurrence by using high-spatial-resolution signal enhancement ratio imaging,” *Radiology*, vol. 248, no. 1, pp. 79–87, 2008.

[67] Nazia F Jafri, David C Newitt, John Kornak, Laura J Esserman, Bonnie N Joe, and Nola M Hylton, “Optimized breast mri functional tumor volume as a biomarker of recurrence-free survival following neoadjuvant chemotherapy,” *Journal of Magnetic Resonance Imaging*, vol. 40, no. 2, pp. 476–482, 2014.

[68] David Newitt, Nola Hylton, et al., “Multi-center breast dce-mri data and segmentations from patients in the i-spy 1/acrion 6657 trials,” *Cancer Imaging Arch*, vol. 10, no. 7, pp. 2016, 2016.